Title

Assessment of perivascular space morphometry across the white matter in Huntington's disease using MRI.

Authors

Annabelle Coleman[a], Mackenzie T. Langan[b,c], Gaurav Verma[c], Harry Knights[a], Aaron Sturrock[d], Blair R. Leavitt[d], Sarah J. Tabrizi[a], Rachael I. Scahill[a], Nicola Z. Hobbs[a].

Author Affiliations

[a] Department of Neurodegenerative Disease, UCL Institute of Neurology, University College London, London, United Kingdom.

[b] Icahn School of Medicine at Mount Sinai, New York, NY, United States.

[c] Biomedical Engineering and Imaging Institute at Mount Sinai School of Medicine, New York, NY, United States.

[d] Department of Medical Genetics, Centre for Molecular Medicine and Therapeutics, University of British Columbia, Vancouver, British Columbia, Canada.

Running title (45 characters including spaces)

White matter PVS morphometry in HD using MRI

Corresponding author contact details

Annabelle Coleman, email: annabelle.coleman.21@ucl.ac.uk, address: Huntington's Disease Centre, UCL Queen Square Institute of Neurology, 2nd Floor Russell Square House, 10-12 Russell Square, London, WC1B 5EH.

Abstract

Background:

Perivascular spaces (PVS) are fluid-filled cavities surrounding small cerebral blood vessels. There are limited reports of enlarged PVS across the grey matter in manifest Huntington's disease (HD). Little is known about how PVS morphometry in the white matter may contribute to HD. Enlarged PVS have the potential to both contribute to HD pathology and affect the distribution and success of intraparenchymal and intrathecally administered huntingtin-lowering therapies.

Objective:

To investigate PVS morphometry in the global white matter across the spectrum of HD. Relationships between PVS morphometry and disease burden and severity measures were examined.

Methods:

White matter PVS were segmented on 3T T2W MRI brain scans of 33 healthy controls, 30 premanifest HD (pre-HD), and 32 early manifest HD (early-HD) participants from the Vancouver site of the TRACK-HD study. PVS count and total PVS volume were measured.

Results:

PVS total count slightly increased in pre-HD (p=0.004), and early-HD groups (p=0.005), compared to healthy controls. PVS volume, as a percentage of white matter volume, increased subtly in pre-HD

compared to healthy controls (p=0.044), but not in early-HD. No associations between PVS measures and HD disease burden or severity were found.

Conclusions:

This study reveals relatively preserved PVS morphometry across the global white matter of pre-HD and early-HD. Subtle morphometric abnormalities are implied but require confirmation in a larger cohort. However, in conjunction with previous publications, further investigation of PVS in HD and its potential impact on future treatments, with a focus on subcortical grey matter, is warranted.

Keywords:

Huntington's disease; magnetic resonance imaging; perivascular spaces; PVSSAS.

Introduction

Huntington's disease (HD) is an autosomal dominant neurodegenerative disease caused by a cytosine-adenine-guanine (CAG) trinucleotide repeat expansion in the huntingtin (*HTT*) gene for which there is currently no cure [1]. Despite this, the single genetic cause of HD has led to the development of a diverse pipeline of clinical trials aiming to lower mutant *HTT* (mHTT) [2]. Many of these putative treatments are administered either intrathecally, such as antisense oligonucleotides, or via intraparenchymal delivery such as genetic therapies [3]. Understanding factors that may affect regional distribution and success of such therapies throughout the grey and white matter, such as morphological changes in perivascular spaces (PVS), is imperative [3]. Thus, a more in-depth understanding of PVS, particularly in premanifest (pre-HD) and early manifest HD (early-HD), may facilitate future clinical trial design or interpretation.

PVS are fluid-filled structures surrounding the walls of arterioles, capillaries, and venules within the brain parenchyma and throughout the white matter [4]. Astrocytic end-feet containing aquaporin-4 (AQP-4) channels make up the external boundary, and the vessel wall forms the internal boundary of

PVS. While their precise role remains elusive, they are believed to act as a conduit for fluid transport, including the exchange of cerebrospinal fluid (CSF) surrounding the cortex with intra-parenchymal interstitial fluid [5]. This exchange facilitates waste clearance from the brain and contributes to the maintenance of brain homeostasis [6]. By contrast, increased PVS load is associated with neuroinflammation [7], blood-brain barrier (BBB) dysfunction, and impaired clearance from the interstitial space, ultimately leading to the accumulation of toxins and hypoxia, causing tissue damage [6]. There is evolving interest in abnormal PVS morphometry in neurological disorders and how they contribute to disease mechanisms with numerous strategies and techniques proposed in the literature to enhance the visibility and quantification of PVS. For example, there are reports of visibly enlarged PVS (ePVS) on magnetic resonance imaging (MRI) in various neurological diseases including Alzheimer's disease [8], small vessel disease [6], multiple sclerosis [9], and HD [3,10–12].

PVS in HD have mostly been investigated in subcortical grey matter structures in participants with manifest disease. Using PVS visual scores on 1.5T MRI, one study found increased PVS burden in the basal ganglia of manifest HD participants compared to first-degree relatives [10]. A histological study found profoundly enlarged PVS on *ex vivo* 7T MRI in HD participants. However, the authors acknowledged that whether ePVS were a fault of fixation artefact or a disease-specific observation was unknown [11]. Subsequently, an *in vivo* 3T MRI study reported a larger percentage volume of dilated PVS in subcortical structures in early-HD participants compared to healthy controls [3]. They reported higher PVS burden to be associated with smaller caudate volume, suggesting PVS burden becomes progressively worse with increasing disease severity; however, this is only suggestive because the study was cross-sectional [3]. Furthermore, a greater quantity of ePVS has been shown to overlap with areas of impaired cerebrovascular reactivity in HD participants compared to controls [12]. This can alter cerebral blood flow and induce relative hypoxia, therefore, compromising PVS function and encouraging enlargement of PVS. A relationship between cerebrovascular reactivity and PVS suggests that neurovascular alterations in HD have the potential to contribute to the enlargement of PVS.

Nonetheless, the reasons for the widening of PVS remain to be elucidated but they may be an indication of compromised PVS function. A review by Brown, et al., (2018) described obstruction of PVS from protein and cell debris to contribute to the widening of PVS and stagnation of fluid drainage [6]. HD is a disease caused by the accumulation of mHTT protein [13] and there have been reports that clearance of mHTT occurs through PVS in the glymphatic system [14]. This suggests that mHTT might amass within PVS, leading to detectable PVS enlargement on 3T MRI, potentially due to the accumulation of debris around vascular cells [6]. This postulation would need to be investigated further as enlarged PVS have the potential to affect the distribution and success of intraparenchymal and intrathecally-administered therapies in HD [2].

Additionally, a recent study examined the glymphatic distribution of antisense oligonucleotides (ASOs) in BACHD transgenic mice expressing the human HTT gene [15]. They found that, following cisternal injection, ASOs entered the brain parenchyma via PVS in the cortex and striatum of mice. This study also found downregulation of AQP-4 in astrocytes decreased levels of ASOs in the brain, suggesting AQP-4 lined PVS are vital for intracisternal injected therapies [15]. Therefore, further understanding of PVS morphological alterations across the spectrum of HD will enable a deeper understanding of how they could impact future HD therapies.

PVS are very small structures and manually identifying and delineating them is extremely time-consuming and prone to rater error [16]. Despite this, multiple different automated and semi-automated pipelines for PVS quantification have been described in the literature based on classical image processing techniques or machine learning approaches to eliminate time-consuming manual processes [17]. For example, the effectiveness of employing a Frangi filter for detecting tubular structures in semi- and fully automated methods have been investigated, resulting in successful and robust segmentation of PVS through the extraction of a vesselness map derived from the tubular morphology characteristics of PVS [18–20]. Furthermore, various machine learning approaches have been investigated, where algorithms are trained with manually labeled PVS segmentations; through

multiple iterations, these models learn the features associated with PVS and can subsequently label PVS structures on new data [17]. For instance, Park et al., (2016) demonstrated a machine-learning technique utilizing random forests for automated PVS segmentation [21]. More recently, efforts have been focused on enhancing the visibility of PVS on scans. One approach combined both T1- and T2-weighted images to achieve enhanced PVS contrast (EPC), making the PVS clusters more discernible from the white matter [22]. However, the availability of such techniques are often limited, with the majority being in-house techniques [19].

Recently, perivascular space semi-automatic segmentation (PVSSAS) [23], was made freely available on GitHub (https://github.com/smithd37/pvssas) for segmenting, viewing, and editing PVS *in vivo* on T2-weighted scans across the cortical white matter. PVSSAS quantifies PVS count, PVS total volume (mm^3) and PVS median long and short axis (mm). This method was validated on a participant with multiple sclerosis, finding an 83% overlap of PVS detected manually and using PVSSAS [16], and has since been applied to quantify PVS across the white matter in participants with COVID-19 [23] and major depressive disorder patients [24].

The objective of this study is to assess the application of PVSSAS, an existing analysis pipeline validated for quantification of PVS in T2-weighted images across the global white matter, for use in HD using a cohort of pre-HD, early-HD, and matched controls. The clinical application of this method will investigate PVS morphometry in the global white matter across the spectrum of HD to visualize if there is a stepwise increase in total PVS count and absolute PVS volume from controls to pre-HD to early-HD. Additionally, we will assess the relationships between PVS morphology and measures of disease burden/severity in HD including HD disease burden score (DBS) and total motor score (TMS).

Materials and methods

Study participants

Participant data from the Vancouver site of the multi-site TRACK-HD study were selected [25–28] including 33 healthy controls, 30 pre-HD, and 32 early-HD participants. Participants were aged 18 to 65 years, able to tolerate MRI and biosample collection, and without major psychiatric disorder or previous significant head injury. Written informed consent was obtained from each participant according to the Declaration of Helsinki and this study was approved by local ethics committees. Full descriptions of data collection, storage, procedures, ethical approval, and demographics are found in previous TRACK-HD publications [25–28].

Healthy controls included siblings, relatives, and non-family members with confirmed non-expanded CAG repeat lengths. Controls were recruited with comparable environmental and social exposures with HD participants as well as some psychological burdens of living with HD [25]. Pre-HD participants (prior to clinical onset) required a CAG repeat expansion of $\geq$40 and a DBS of >250 which approximates 15 years to estimated disease onset [29]. DBS is a model to reflect the burden of HD pathology determined by age x (CAG – 35.5) [30]. A Unified Huntington's Disease Rating Scale (UHDRS) TMS of $\leq$5 to indicate a lack of significant motor features was required for pre-HD participants [25]. Early-HD participants (clinical motor onset) required a CAG repeat expansion of $\geq$40 and were identified in stage 1 or 2 according to the Shoulson and Fahn staging system with a UHDRS Total Functional Capacity (TFC) score of $\geq$7 [31].

Image acquisitions

Participants underwent both T1-weighted (T1) and T2-weighted (T2) MRI in the same visit. For T1 scans, a 3D MPRAGE acquisition on 3T Phillips scanners with the following imaging parameters was used: TE = 3.5ms, TR = 7.7ms, FA = 8°, FOV = 24cm, matrix size = 224x224, voxel size = 1.07x1.07x1.07mm^3. A total of 164 sagittal slices were produced for each scan with 1.0mm slice thickness. For T2 scans, a VISTA sequence was used for the 3T Phillips scanners with an identical field of view, acquisition matrix and slice thickness as T1 scans [25].

Perivascular space analysis pipeline

The analysis pipeline for PVS segmentation included MRI pre-processing, PVS morphometric measurements, and refinement of the methodology (Figure 1). This included parameter optimisation for this 3T cohort from the Vancouver site and reproducibility testing to assess manual edits to improve segmentation accuracy. We utilized a single TRACK-HD cohort site for this exploratory analysis to mitigate confounding variables, as site-specific optimization is necessary for PVSSAS software. Prior to running MRI data through the pipeline, raw T1 and T2 data were visually inspected for artefacts and those deemed unsuitable for analysis were excluded prior to processing.

MRI pre-processing

T1 and T2 scans that passed visual quality control were co-registered using Statistical Parametric Mapping version 12 (SPM12) [32] to correct for subtle alignment differences between scans (Figure 1a). This was followed by a dual-channel tissue segmentation within SPM12 to generate a white matter mask using default parameters for bias regularisation and bias full-width half maximum. SPM12's built-in dual-channel segmentation segments, bias corrects, and spatially normalises all in the same model [32]. This segmentation method combined the different T1 and T2 image contrasts to generate a white matter mask that was specific to the T2 images (Figure 1b). Additional morphological pre-processing steps included optimising the white matter mask for PVSSAS which can be found in Supplementary Material 1 (Figure 1c). The quality of white matter masks was visually inspected and those deemed unsuitable for analysis were excluded prior to processing.

PVS morphometric measurements

PVSSAS is a semi-automated segmentation tool for segmenting, viewing, and editing PVS *in vivo* [23]. It functions to segment PVS in T2 images by using a 2D Frangi-based detection algorithm: a quick and powerful segmentation technique to detect vessel-like structures and fibers in volumetric data, such as PVS [20]. PVSSAS pipeline refinement and the reproducibility of PVS segmentations were assessed and the methods for this can be found in Supplementary Material 2. To summarise, Frangi filter parameter optimisation included systematically assessing each parameter gradually within their pre-defined limits and visually inspecting the PVS segmentations. Supplementary Table A summarises the different parameters, the range explored for the optimisation process in this study, and how they change PVS segmentations. The final PVSSAS parameters were used: PVSSAS filter size to 0.5-10, Frangi scale range of [0.5-3.2], scale ratio of 2, Frangi $\beta 1$ to 0.98, Frangi $\beta 2$ to 0.35.

For each participant, the T2 image and white matter mask were inserted into PVSSAS and PVS were segmented (Figure 1d-1e). MRI scans in PVSSAS can only be viewed in one plane at a time, restricting the view of PVS. To increase the reliability of the visual quality control of the segmented and non-segmented PVS, FMRIB Software Library (FSL) viewer [33] was open with the corresponding T2 scan for additional 3-plane visibility of PVS.

Manually editing, adding, and removing PVS on PVSSAS included removing PVS outside the white matter mask such as within a ventricle or sulcus. Missegmented white matter hyperintensities were removed. PVS that were not segmented by PVSSAS were added in all visible slices above and below using the 'Add' tool if they were visible on FSLView and abided by the STRIVE criteria (Figure 1e) [34].

Statistical analysis

All data analysis was performed using STATA version 17.0 (https://www.stata.com). The level of significance for all statistical tests was set at 0.05. Appropriate normality tests were performed, and log transformations were attempted for variables where necessary.

Demographic group differences were investigated using independent t-tests for normally distributed data and Mann-Whitney U tests when groups were not normally distributed. A Chi-squared test was used for group differences in sex.

For the main analysis, absolute group differences for PVS count and PVS volume were assessed using linear regression with age, sex, and total intracranial volume (TIV) adjusted for as nuisance variables. Further analysis looked at the density of PVS count and PVS volume in the white matter by normalising to white matter volume. PVS count density was calculated as PVS count per $1000mm^3$ of white matter volume. PVS volume was calculated as a percentage of white matter volume: total PVS volume divided by total white matter volume. Group differences between healthy controls, pre-HD and early-HD for these variables were assessed using linear regression models with age, sex, and TIV as nuisance variables.

Linear regression analyses were conducted to investigate associations between PVS variables with TMS and DBS with age, sex, and TIV adjusted for nuisance variables. TMS was only assessed in early-HD participants as most pre-HD participants would score at floor level. DBS was used as a disease burden measure across all gene-positive participants and, therefore, comprised both pre-HD and early-HD participants.

Results

Group demographics

Table 1 provides demographic data for the participants included in this study. As expected for a progressive disease, pre-HD participants were significantly younger than early-HD participants (p=0.004). The distribution of males and females differed slightly between groups as assessed by a chi-squared test ($\chi 2$=6.38, p=0.041). DBS, TMS, and TFC all showed a significant increase between pre-HD

and early-HD groups (as expected for a progressive disease) whereas CAG repeat length did not differ between HD groups (p=0.464).

Quality control

Visual assessment of T1 and T2 scans excluded three participants due to motion artefact (1/33 healthy controls, 1/30 pre-HD, 1/32 early-HD). Following processing, four participants were excluded due to white matter mask failure; two failures from over-segmented non-cortical areas (2/33 healthy controls), and two from over-segmentation of the brainstem (1/33 healthy controls, 1/30 pre-HD). After discussion, one pre-HD participant was excluded due to overwhelming additional small vessel disease features, making the differentiation and delineation of PVS difficult due to additional non-HD pathology. The final cohort used for statistical analysis included 29 healthy controls, 27 pre-HD and 31 early-HD with a total failure rate of 8%. No patterns of systematic failure between HD and healthy controls were identified.

PVSSAS between-group differences

The reproducibility of the manual refinement of the PVSSAS segmentations was assessed and intraclass correlation coefficient (ICC) values for all PVS metrics included in this study were 0.95 or higher, showing excellent reproducibility of the manual refinement process for all PVS measures (Supplementary Table B). See supplementary Material 2 for further information about reproducibility tests and results.

White matter volume was significantly smaller in early-HD compared with both healthy controls and pre-HD, as expected ($p<0.0005$ for both, Table 3), adjusted for age, sex and TIV. No significant difference was found in white matter volume between pre-HD and healthy controls in this relatively small cohort (Table 2).

Absolute PVS count was on average 8.1% higher in pre-HD compared to healthy controls (p=0.027), adjusted for age, sex and TIV. Although the mean PVS count in early-HD was similar to pre-HD (mean of 278 and 279, respectively, Table 2), it was not statistically significantly different between early-HD and healthy controls (p=0.23), most likely due to higher standard deviation in early-HD. Overall, absolute PVS count shows large overlap between groups with considerable variability in the data (Figure 2A).

PVS count density was statistically significantly higher in both pre-HD (8.2% on average) and early-HD (16.4% on average) compared to healthy controls (p=0.004 and p=0.005, respectively; Table 3; Figure 2B), adjusted for age, sex and TIV. Differences between the two HD groups were small and non-significant (p=0.92).

Absolute PVS volume was not statistically significant between groups (Table 3, Figure 2C). However, there was a statistically significant increase in PVS volume as a percentage of white matter in pre-HD compared to healthy controls (9.1% increase in pre-HD on average; p=0.044, Table 3), adjusted for age, sex and TIV. Although the mean PVS volume (as a percentage of white matter volume) also increased in early-HD compared with healthy controls, the mean difference was not statistically significant (Table 3) and there is considerable overlap in the data (Figure 2D).

Relationship between PVS measures and burden/severity measures of HD

As PVS count density and PVS volume (as a percentage of white matter volume) yielded significant results between healthy controls and HD groups (Table 3), further exploration of these variables and their association with measures of disease burden and severity in HD were assessed. This included DBS in both HD groups combined and TMS in early-HD (Supplementary Table E). There were no statistically significant relationships between PVS measures and DBS in both pre-HD and early-HD

participants combined or between PVS measures and TMS in early-HD participants (Supplementary Table E).

Discussion

Few studies have explored PVS in both pre-HD and early-HD individuals and across the white matter with this being the first study to apply a semi-automated PVS segmentation tool to part of the TRACK-HD cohort. We assessed PVS metrics in healthy controls, pre-HD and early-HD participants and sought to explore the relationships between PVS measures with HD DBS and motor function. Overall, there were no marked abnormalities in PVS morphometry in the white matter of both pre-HD and early-HD individuals in this study. Subtle morphometric abnormalities are implied but require confirmation in a larger cohort. We found PVS count, PVS count density and PVS volume (as a percentage of white matter volume) to be subtly statistically significantly higher in pre-HD participants compared to healthy controls. Early-HD participants showed subtle statistically significantly higher PVS count density compared to controls. No associations between PVS measures with HD DBS and motor function were found.

The main findings of this study show a statistically significant increase in absolute PVS count, PVS count density and PVS total volume (as a percentage of white matter volume) in the white matter of pre-HD participants compared to healthy controls. Group differences in early-HD compared with controls were similar in direction and magnitude to pre-HD compared with controls, but only reached statistical significance for PVS count density over the white matter. The underlying causes of subtle increases in PVS enlargement in HD are unknown, however, HD is a disease caused by the accumulation of mHTT protein [13] and there have been reports that clearance of mHTT occurs through PVS in the glymphatic system [14]. This suggests that mHTT might amass within PVS, leading to detectable PVS enlargement on 3T MRI, potentially due to the accumulation of debris around vascular cells [6]. This postulation would need to be investigated, for example, using positron emission tomography (PET) radiotracers

to track mHTT through the glymphatic system to identify any accumulation in PVS. One limitation of this proposed investigation is that no PET tracer targeting mHTT has been fully validated to date [35]; although, much work is currently underway in this area [36].

Previous studies have indicated ePVS potentially contributes to HD pathologies. Both BBB dysfunction and impaired cerebrovascular reactivity (CVR) have previously been reported as pathological consequences of ePVS in small vessel disease [6], and both neurovascular impairments have been reported in participants with HD [12,37]. This is speculative but suggests a bidirectional link between BBB dysfunction, impaired CVR, and ePVS in HD. While exploring the connection between BBB dysfunction and ePVS in HD requires further investigation, recent research examined CVR in relation to PVS and identified regional CVR impairments in subcortical white matter regions among pre-HD and early-HD participants [12]. The authors reported greater dilated PVS load to overlap with subcortical white matter regions showing reduced CVR, which could be due to reductions in cerebral blood flow and hypoxia, resulting in increased PVS burden [12]. This differs from our study's findings, which revealed only subtle volumetric PVS changes.

Our study has several limitations. Inclusion of manual intervention allows correction of automated segmentation errors, but user-error risk increases. Whilst we showed excellent intra-rater reliability, same-scan differences remain and reproducibility is critically dependent on rater expertise. Fully automated techniques have the advantage of efficiency and consistency which makes them practical for large datasets, but segmentation errors may be problematic particularly when anatomy deviates from normality e.g., due to atrophy or other pathology. For example, a recent study used a fully automated computational quantification method to assess PVS in the centrum semiovale of 700 participants from the 1936 Lothian Birth Cohort [18]. Since manual refinement of segmentations was not possible, 23% of the cohort was excluded due to falsely segmented artefacts [18]. Fully automated methods are superior for efficient and consistent analysis in large datasets, however, if a large amount

of the cohort is excluded due to the inability to refine segmentations, then a semi-automated method could be advantageous.

That being acknowledged, our study was limited by the small sample size, hence it could be considered a pilot study. However, the use of a smaller sample facilitated the parameter optimization process for PVSSAS, as site-specific parameter optimisation is necessary for this technique. This is time-consuming and could be difficult to standardise for multi-site studies [19]. Therefore, for this study, we only used one site of the TRACK-HD cohort.

Prior research has observed a more substantial increase in PVS volume within subcortical grey matter structures in HD compared to the findings in the global white matter in this study [3], suggesting that PVS morphometry may be relatively preserved in the white matter in HD and more pronounced in the grey matter. PVSSAS was developed and validated for the quantification of PVS in T2-weighted images across the global white matter [16]. This software was selected for the current study as our focus was to investigate PVS abnormalities over the white matter – an area that has been relatively underexplored for PVS in HD, despite the fact that pronounced white matter changes, e.g., atrophy, are evident early in the course of the disease [25–28]. The results from our study suggest that PVS morphological changes over the white matter appear to be much more subtle compared to PVS findings in subcortical grey matter in early-HD found in other studies. Because of this, we would recommend that further work focuses on PVS in the grey matter to understand the impact of PVS in the striatum where pathological alterations begin earliest in the disease [38].

Acknowledgements

The authors would like to thank the participants who took part in this study.

Funding

The TRACK-HD study was funded by CHDI. SJT is partly supported by the UK Dementia Research Institute which receives its funding from DRI Ltd., funded by the UK Medical Research Council, Alzheimer's Society, and Alzheimer's Research UK. SJT holds a Wellcome Trust research grant (ref. 223082/Z/21/Z) which provides funding for RIS and NZH. AC is funded by the Medical Research Council (ref. MR/W026686/1).

Conflict of Interest

Blair R. Leavitt is an Editor-in-chief and Sarah J. Tabrizi is an Associate Editor of this journal, but they were not involved in the peer-review process nor had access to any information regarding its peer-review.

Data availability

The data supporting the findings of this study are available on request from the corresponding author. The data are not publicly available due to privacy, ethical restrictions, or other concerns.

References

1. MacDonald ME, Ambrose CM, Duyao MP, Myers RH, Lin C, Srinidhi L, et al. A novel gene containing a trinucleotide repeat that is expanded and unstable on Huntington's disease chromosomes. The Huntington's Disease Collaborative Research Group. Cell. 1993 Mar 26;72(6):971–83.
2. Estevez-Fraga C, Tabrizi SJ, Wild EJ. Huntington's Disease Clinical Trials Corner: August 2023. J Huntingtons Dis. 2023;2(2):169.
3. Chan ST, Mercaldo ND, Ravina B, Hersch SM, Rosas HD. Association of Dilated Perivascular Spaces and Disease Severity in Patients With Huntington Disease. Neurology. 2021 Feb 2;96(6):e890.

4. Wardlaw JM, Benveniste H, Nedergaard M, Zlokovic B V., Mestre H, Lee H, et al. Perivascular spaces in the brain: anatomy, physiology and pathology. Nat Rev Neurol. 2020 Mar 1 16(3):137–53.

5. Jessen NA, Munk ASF, Lundgaard I, Nedergaard M. The Glymphatic System – A Beginner's Guide. Neurochem Res. 2015 Dec 1;40(12):2583.

6. Brown R, Benveniste H, Black SE, Charpak S, Dichgans M, Joutel A, et al. Understanding the role of the perivascular space in cerebral small vessel disease. Cardiovasc Res. 2018 Sep 1;114(11):1462–73.

7. Ineichen B V., Okar S V., Proulx ST, Engelhardt B, Lassmann H, Reich DS. Perivascular spaces and their role in neuroinflammation. Neuron. 2022 Nov 2;110(21):3566–81.

8. Vilor-Tejedor N, Ciampa I, Operto G, Falcón C, Suárez-Calvet M, Crous-Bou M, et al. Perivascular spaces are associated with tau pathophysiology and synaptic dysfunction in early Alzheimer's continuum. Alzheimers Res Ther [Internet]. 2021 Dec 1;13(1):1–13.

9. Liu XY, Ma GY, Wang S, Gao Q, Guo C, Wei Q, et al. Perivascular space is associated with brain atrophy in patients with multiple sclerosis. Quant Imaging Med Surg. 2022 Feb 1;12(2):1004.

10. Valdés Hernández M del C, Abu-Hussain J, Qiu X, Priller J, Parra Rodríguez M, Pino M, et al. Structural neuroimaging differentiates vulnerability from disease manifestation in colombian families with Huntington's disease. Brain Behav. 2019 Aug 1;9(8).

11. Bulk M, Hegeman-Kleinn I, Kenkhuis B, Suidgeest E, van Roon-Mom W, Lewerenz J, et al. Pathological characterization of T2*-weighted MRI contrast in the striatum of Huntington's disease patients. Neuroimage Clin. 2020 Jan 1;28:102498.

12. Chan ST, Mercaldo ND, Kwong KK, Hersch SM, Rosas HD. Impaired Cerebrovascular Reactivity in Huntington's Disease. Front Physiol. 2021 Jul 21;12.

13. DiFiglia M, Sapp E, Chase KO, Davies SW, Bates GP, Vonsattel JP, et al. Aggregation of huntingtin in neuronal intranuclear inclusions and dystrophic neurites in brain. Science. 1997 Sep 26;277(5334):1990–3.

14. Caron NS, Banos R, Yanick C, Aly AE, Byrne LM, Smith ED, et al. Mutant Huntingtin Is Cleared from the Brain via Active Mechanisms in Huntington Disease. J Neurosci. 2021 Jan 27;41(4):780–96.

15. Wu T teng, Su F juan, Feng Y qing, Liu B, Li M yue, Liang F yin, et al. Mesenchymal stem cells alleviate AQP-4-dependent glymphatic dysfunction and improve brain distribution of antisense oligonucleotides in BACHD mice. Stem Cells. 2020 Feb 1;38(2):218–30.

16. Smith DA, Verma G, Ranti D, Markowitz M, Balchandani P, Morris L. Perivascular Space Semi-Automatic Segmentation (PVSSAS): A Tool for Segmenting, Viewing and Editing Perivascular Spaces. bioRxiv. 2020 Nov 17;2020.11.16.385336.

17. Pham W, Lynch M, Spitz G, O'Brien T, Vivash L, Sinclair B, et al. A critical guide to the automated quantification of perivascular spaces in magnetic resonance imaging. Front Neurosci. 2022 Dec 14;16:1021311.

18. Ballerini L, Booth T, Valdés Hernández M del C, Wiseman S, Lovreglio R, Muñoz Maniega S, et al. Computational quantification of brain perivascular space morphologies: Associations with

vascular risk factors and white matter hyperintensities. A study in the Lothian Birth Cohort 1936. Neuroimage Clin. 2020 Jan 1;25:102120.

19. Ballerini L, Lovreglio R, Valdés Hernández MDC, Ramirez J, MacIntosh BJ, Black SE, et al. Perivascular Spaces Segmentation in Brain MRI Using Optimal 3D Filtering. Scientific Reports 2018 8:1. 2018 Feb 1;8(1):1–11.

20. Frangi AF, Niessen WJ, Vincken KL, Viergever MA. Multiscale vessel enhancement filtering. Lecture Notes in Computer Science (including subseries Lecture Notes in Artificial Intelligence and Lecture Notes in Bioinformatics). 1998;1496:130–7.

21. Park SH, Zong X, Gao Y, Lin W, Shen D. Segmentation of perivascular spaces in 7 T MR image using auto-context model with orientation-normalized features. Neuroimage. 2016 Jul 1;134:223–35.

22. Sepehrband F, Barisano G, Sheikh-Bahaei N, Cabeen RP, Choupan J, Law M, et al. Image processing approaches to enhance perivascular space visibility and quantification using MRI. Scientific Reports 2019 9:1. 2019 Aug 26;9(1):1–12.

23. Langan MT, Smith DA, Verma G, Khegai O, Saju S, Rashid S, et al. Semi-automated Segmentation and Quantification of Perivascular Spaces at 7 Tesla in COVID-19. Front Neurol. 2022 Apr 1;13:846957.

24. Ranti DL, Warburton AJ, Rutland JW, Dullea JT, Markowitz M, Smith DA, et al. Perivascular spaces as a marker of psychological trauma in depression: A 7-Tesla MRI study. Brain Behav. 2022 Jul 1;12(7).

25. Tabrizi SJ, Langbehn DR, Leavitt BR, Roos RA, Durr A, Craufurd D, et al. Biological and clinical manifestations of Huntington's disease in the longitudinal TRACK-HD study: cross-sectional analysis of baseline data. Lancet Neurol. 2009 Sep;8(9):791–801.

26. Tabrizi SJ, Scahill RI, Durr A, Roos RAC, Leavitt BR, Jones R, et al. Biological and clinical changes in premanifest and early stage Huntington's disease in the TRACK-HD study: the 12-month longitudinal analysis. Lancet Neurol. 2011 Jan;10(1):31–42.

27. Tabrizi SJ, Reilmann R, Roos RAC, Durr A, Leavitt B, Owen G, et al. Potential endpoints for clinical trials in premanifest and early Huntington's disease in the TRACK-HD study: analysis of 24 month observational data. Lancet Neurol. 2012 Jan;11(1):42–53.

28. Tabrizi SJ, Scahill RI, Owen G, Durr A, Leavitt BR, Roos RA, et al. Predictors of phenotypic progression and disease onset in premanifest and early-stage Huntington's disease in the TRACK-HD study: Analysis of 36-month observational data. Lancet Neurol. 2013 Jul;12(7):637–49.

29. Langbehn DR, Brinkman RR, Falush D, Paulsen JS, Hayden MR. A new model for prediction of the age of onset and penetrance for Huntington's disease based on CAG length. Clin Genet. 2004 Apr;65(4):267–77.

30. Penney JB, Vonsattel JP, MacDonald ME, Gusella JF, Myers RH. CAG repeat number governs the development rate of pathology in Huntington's disease. Ann Neurol. 1997 May;41(5):689–92.

31. Shoulson I, Fahn S. Huntington disease: clinical care and evaluation. Neurology. 1979;29(1):1–3.

32. Ashburner J, Friston KJ. Unified segmentation. Neuroimage. 2005 Jul 1;26(3):839–51.

33. Jenkinson M, Beckmann CF, Behrens TEJ, Woolrich MW, Smith SM. FSL. Neuroimage. 2012 Aug;62(2):782–90.

34. Wardlaw JM, Smith EE, Biessels GJ, Cordonnier C, Fazekas F, Frayne R, et al. Neuroimaging standards for research into small vessel disease and its contribution to ageing and neurodegeneration. Lancet Neurol. 2013 Aug;12(8):822–38.

35. Cybulska K, Perk L, Booij J, Laverman P, Rijpkema M. Huntington's Disease: A Review of the Known PET Imaging Biomarkers and Targeting Radiotracers. Molecules. 2020 Jan 23;25(3).

36. Bertoglio D, Verhaeghe J, Miranda A, Wyffels L, Stroobants S, Mrzljak L, et al. Longitudinal preclinical evaluation of the novel radioligand [11C]CHDI-626 for PET imaging of mutant huntingtin aggregates in Huntington's disease. Eur J Nucl Med Mol Imaging. 2022 Mar 1;49(4):1166–75.

37. Drouin-Ouellet J, Sawiak SJ, Cisbani G, Lagacé M, Kuan WL, Saint-Pierre M, et al. Cerebrovascular and blood-brain barrier impairments in Huntington's disease: Potential implications for its pathophysiology. Ann Neurol. 2015 Aug 1;78(2):160–77.

38. Bates GP, Dorsey R, Gusella JF, Hayden MR, Kay C, Leavitt BR, et al. Huntington disease. Nat Rev Dis Primers. 2015 Apr 23;1.

Tables

Table 1 – Group demographics.

	Controls (n=29) Mean (SD)	Pre-HD (n=27) Mean (SD)	Early-HD (n=31) Mean (SD)	*p*-value
Age (years)	46.1 (11.9)	39.1 (10.2)	47.9 (22.8)	**0.041**[1], 0.62[2], **0.004**[3]
Sex (%M)	41.4	44.4	71	**0.041**[+]
TIV (mm3)	1466758 (140953)	1480589 (167905)	1463700 (132841)	0.98[1], 0.057[2], 0.075[3]
CAG Length	-	43.4 (2.5)	44.7 (4.2)	0.46[3]
DBS	-	287 (43.5)	403 (76.5)	**0.00005**[3]
TMS	-	2.6 (1.2)	30 (9.8)	**0.00005**[3]
TFC	-	12.8 (0.8)	10.1 (2.1)	**0.00005**[3]

Table 1: Data are mean (SD). Demographic data of the participants that were included in the analysis. Age and CAG length used a Mann-Whitney U test. All other group differences are found using an independent t-test apart from a chi-squared test to assess sex group differences. Bold values are statistically significant (p<0.05).

[1]Control versus pre-HD, [2]Control versus early-HD, [3]Pre-HD versus early-HD, [+]Chi-squared test.

Abbreviations: SD, standard deviation; M, males; TIV, total intracranial volume; CAG, trinucleotide repeat number; DBS, disease burden score; TMS, total motor score; TFC, total functional capacity.

Table 2 – Group summary statistics of PVS measures.

	Control (n=29) Mean (SD)	Pre-HD (n=27) Mean (SD)	Early-HD (n=31) Mean (SD)
White matter volume (mm^3)	425397 (48724)	424453 (60498)	391662 (44194)
PVS total count	258 (63.2)	279 (48.4)	278 (61.1)
PVS total volume (mm^3)	4712 (1855)	5180 (1699)	5077 (1629)
PVS count density (count per 1000 mm^3 WM)	0.61 (0.14)	0.66 (0.12)	0.71 (0.12)
PVS total volume (% of WMV)	1.1 (0.43)	1.2 (0.4)	1.3 (0.41)

Table 2: Summary statistics table of white matter volume and different PVS variables for healthy controls, pre-HD, and early-HD participants. Data are presented as mean and standard deviations (SD). Abbreviations: WMV, white matter volume; WM, white matter.

Table 3 – Mean between-group differences in white matter and PVS metrics.

	Pre-HD - Control (95% CI), *p*	Early-HD - Control (95% CI), *p*	Early-HD – Pre-HD (95% CI), *p*
White matter volume (mm^3)	-944 (-1922 4689), 0.23	**-33735 (-45466 -21836), 0.0005***	**-32791 (-38885 -13891), 0.0005***
PVS total count	**21 (3.7 59.8), 0.027***	20 (-10.9 44.6), 0.23	-1 (-44.2 14.5), 0.32
PVS total volume (mm^3)	468 (-109 1657), 0.085	365 (-577 1169), 0.5	-103 (-1401 445), 0.31
PVS count density (count per 1000 mm^3 WM)	**0.05 (0.03 0.16), 0.004***	**0.1 (0.03 0.15), 0.005***	0.05 (0.07 0.06), 0.92
PVS total volume (% of WMV)	**0.12 (0.006 0.44), 0.044***	0.19 (-0.05 0.38), 0.12	0.07 (-0.28 0.17), 0.64

*Table 3: Table of group mean differences with 95% CIs and corresponding p-values from group linear regressions with age, sex, and TIV controlled for as nuisance variables. *Statistically significant (p<0.05). Abbreviations: CI, confidence interval; WMV, white matter volume; WM, white matter; SD, standard deviation.*

Figures

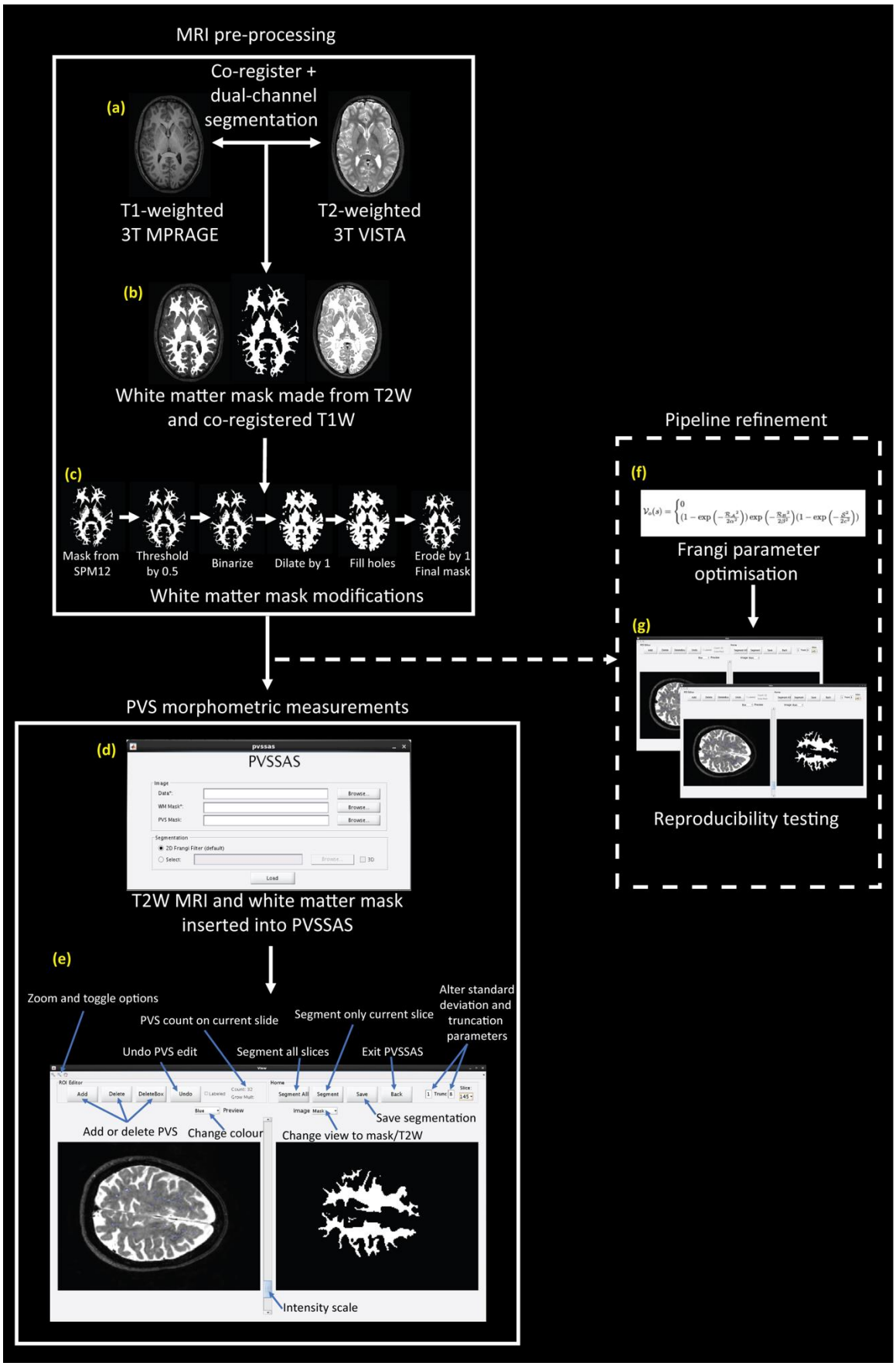
MRI pre-processing
Co-register + dual-channel segmentation
(a)
T1-weighted 3T MPRAGE
T2-weighted 3T VISTA
(b)
White matter mask made from T2W and co-registered T1W
(c)
Mask from SPM12
Threshold by 0.5
Binarize
Dilate by 1
Fill holes
Erode by 1
Final mask
White matter mask modifications
Pipeline refinement
(f)
Frangi parameter optimisation
(g)
Reproducibility testing
PVS morphometric measurements
(d)
PVSSAS
T2W MRI and white matter mask inserted into PVSSAS
(e)
Zoom and toggle options
PVS count on current slide
Segment only current slice
Alter standard deviation and truncation parameters
Undo PVS edit
Segment all slices
Exit PVSSAS
Add or delete PVS
Change colour
Save segmentation
Change view to mask/T2W
Intensity scale

Figure 1: Schematic representing the analysis pipeline including MRI pre-processing, PVS morphometric measurements, and pipeline refinement. (a) T1 MRI co-registered to T2 MRI using SPM12. (b) Dual-channel segmentation was performed on SPM12 using the T2 MRI and the co-registered T1 MRI to generate white matter masks. (c) White matter mask modifications were performed including thresholding by 0.5, binarizing the image, dilating the image by 1 voxel, filling the holes, and eroding the image by 1 voxel to create a final mask (Supplementary Material 1). (d) The PVSSAS interface where each participant's T2 image and white matter masks were inserted. (e) The primary interface of the PVSSAS tool where PVS were automatically segmented in each slice of the scan in the pre-defined white matter and manual editing of the segmentations was performed. (1) Frangi parameters were optimised for use on 3T scans (Supplementary Material 2). (2) Reproducibility of manual edits was examined (Supplementary Material 2).

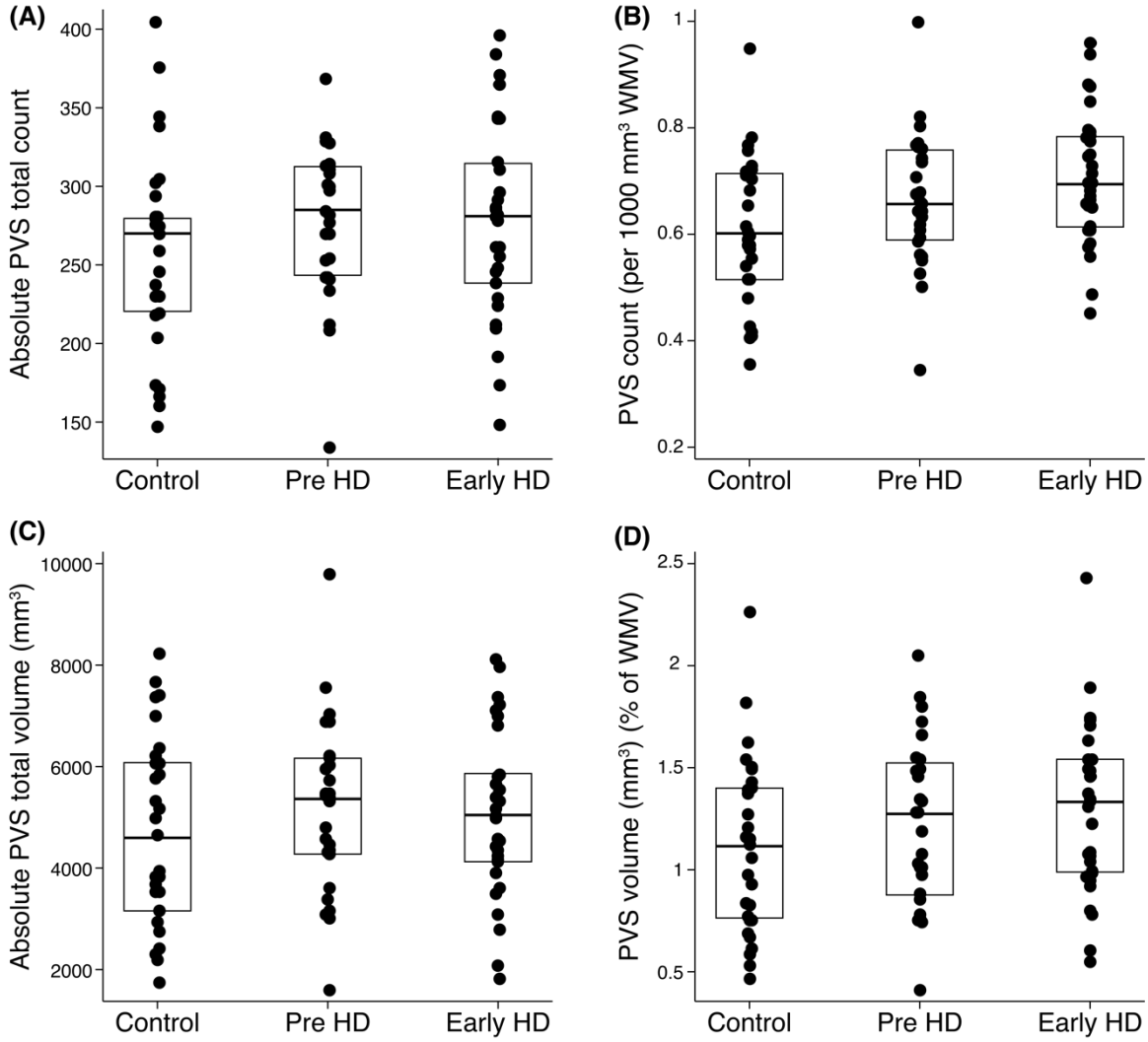

Figure 2: Scatter plots for (A) absolute PVS total count, (B) PVS count density, (C) absolute PVS total volume and (D) PVS volume (as a percentage of white matter volume) between groups with overlayed box plots. Age, sex, and TIV were controlled for as nuisance variables in the regression analysis.

Supplementary Material

Supplementary Material 1 – white matter mask optimisation

Additional morphological pre-processing steps included optimising the white matter mask for PVSSAS (Figure 1c). This included thresholding the white matter mask by 0.5 to exclude all voxels with a probability of <0.5 of being white matter and binarising the image voxels using FSLMaths. The mask was then dilated by 1 voxel and the holes within the mask were filled to create a solid mask including all PVS within the white matter. The mask was eroded by 1 voxel to give a final white matter mask to be inserted into PVSSAS along with the bias-corrected T2 image. The quality of white matter masks was visually inspected and those deemed unsuitable for analysis were excluded prior to processing.

Supplementary Material 2 – PVSSAS pipeline refinement and reproducibility

Pipeline refinement

Parameters for optimisation include the minimum and maximum of the scale range, the scale ratio, Frangi $\beta 1$, and Frangi $\beta 2$. Parameters in [23] were set to a scale range of [1.4-3.2], scale ratio of 2, Frangi $\beta 1$ to 0.95, Frangi $\beta 2$ to 0.35. Parameters for this study were optimised on a subset of the Vancouver data with participants selected to encompass a range of pathology from HC data through to more severe HD pathology (n=3 HCs, n=3 HD). This optimisation cohort was used for parameter optimisation by systematically changing each parameter gradually within their pre-defined limits and visually inspecting the PVS segmentations to determine the 'best fit'. Supplementary Table A summarises the different parameters, the range explored for the optimisation process in this study, and how they change PVS segmentations. Once one parameter was changed, the other parameters were examined again to identify if they could be further optimised with the newly changed parameter.

Supplementary Table A – Parameter optimisation.

Parameter	Function	Range Explored	Effect on PVS Segmentation	Final Parameters
Standard deviation (SD)	Controls how many standard deviations from the mean voxel value the threshold is for detection of a PVS feature.	0.1 – 2.5 with 0.5 increments.	Decreasing SD increased segmentations but decreased PVS accuracy with many false positive PVSs.	1
Scale range	The range PVSs are most likely to be found. Controls the length versus width ratio of an ROI and is the range of sigmas used.	Lower range: 0.1 – 2.0 with 0.1 increments.	Above or below 0.5 reduced PVS segmentations dramatically. Largest effect on PVS count.	0.5
		Upper range: 0.5 – 5.0 with 0.5 increments	No change.	3.2
Scale ratio	Controls step size between sigmas.	0.5 – 4.0 with 0.5 increments.	Increasing scale ratio increased number of false segmentations. Lower than 2 made no change.	2
Frangi *β*1	Corresponds to *α* in Equation 1. Controls the sensitivity of the Frangi filter. Known as Frangi correction constant.	0 .1– 0.9 with 0.1 increments, then 0.9 – 1.0 with 0.01 increments.	Below 0.9 gave fewer PVS segmentations, reduces the sensitivity. More PVSs segmented with increased accuracy using 0.98 and minimal change with higher values.	0.98
Frangi *β*2	Corresponds to *c* in Equation 1. Controls the sensitivity of the Frangi filter. Known as Frangi correction constant.	0.2 – 0.9 with 0.1 increments.	No change.	0.35
Sigma Kernel	The sigma used for the Gaussian kernel.	5 – 8 with increments of 1, default 6.	No change.	6

Supplementary Table A: Summary of the different parameters that were altered for optimisation in this study. The function of the different parameters optimised in this study are explained by Frangi, et al., (1998) and Baboiu & Hamarneh, (2012).

The minimum scale range was the most significant parameter change, which was the same as the parameter optimisation described in Ballerini, et al., (2018). A value of 0.5 was inclusive of more PVS segmentations than any value above or below for this study. Changing the parameter by 0.1 above or below 0.5 decreased the PVS segmentations. The final PVSSAS parameters selected for this study were: PVSSAS filter size to 0.5-10, Frangi scale range of [0.5-3.2], scale ratio of 2, Frangi $\beta 1$ to 0.98, Frangi $\beta 2$ to 0.35.

Reproducibility testing methods

The reproducibility of the PVS segmentations was assessed in three different tests:

Test 1 assessed the reproducibility of the manual refinement of the PVSSAS segmentations. This was performed on a subset of the Vancouver cohort, including examples of healthy control data (n=6) through to more severe HD pathology (n=6). A range of different data was used to ensure manual edits were consistently applied across groups. PVSSAS was run on each of these test scans once, with manual edits performed twice, with a week between each manual edit.

Test 2 aimed to assess scan-rescan reproducibility of PVSSAS algorithm (without manual intervention). The ideal data to assess this would be serial scans acquired during the same scanning session, with the ground truth being that there would be no/negligible change in PVS morphometry between these scans. Any differences in output would be a result of variability in the PVSSAS measurement algorithm itself. Since the TRACK-HD dataset does not have serial repeat scans, feasible data to use is healthy control data with the shortest time interval between scans: 1 year apart. The (imperfect) assumption for using healthy controls is that we would expect minimal change in PVS between serial scans in healthy controls. Thus, 12 healthy control participants (age range 23-66 years) from the Vancouver cohort were selected including data from their first and second visit (scans one year apart). PVSSAS

was run on each 2008 and 2009 scan, without manually editing PVS segmentations, and the output was collected. This method for assessing the reproducibility of PVSSAS presents caveats, however, we believed it to be the most pragmatic approach with the available data.

Test 3 is an extension of Test 2 and assessed the automated algorithm of PVSSAS with the addition of manual edits to understand the contribution of manual refinement to any variability in PVSSAS reproducibility. The same healthy control participants in Test 2 were used in Test 3 with the same assumption that healthy controls would show minimal change in PVS over a year. The procedure was the same as Test 2 but included manual refinement.

To investigate reproducibility, three different reproducibility tests were performed for PVSSAS measurements and were assessed using a two-way mixed-effects model intraclass correlation coefficient (ICC). ICC measures the reliability of PVS measurements in each test with values ranging from 0 to 1 (Koo & Li, 2016). A high ICC close to 1 indicates excellent reliability between PVS measurements and a low ICC value close to 0 indicates PVS metrics in the tests have poor reliability (Koo & Li, 2016).

Reproducibility testing results

Reproducibility was assessed for PVSSAS measurements using two-way mixed-effects model ICCs to assess the reliability of each reproducibility test with values ranging from 0 to 1 where 1 represents complete reliability.

Test 1: Reproducibility of same-scan manual intervention:

The reliability ICC estimates and 95% confidence intervals (CI) to assess the reproducibility of manual edits performed twice on the same scan, one week apart, are represented in Supplementary Table B.

Supplementary Table B – Same-scan manual intervention reproducibility of PVS metrics (Test 1).

	Run 1 (n=12) Mean (SD)	**Run 2 (n=12) Mean (SD)**	**Mean absolute % difference**	**ICC (95% CI), p**
PVS count	243 (39.7)	242 (38.1)	2.2	**0.98 (0.94 0.99), 0.0005***
PVS total volume (mm^3)	4415 (1299)	4325 (1237)	5.7	**0.97 (0.91 0.99), 0.0005***
PVS median long axis (mm)	4.2 (0.4)	4.1 (0.4)	2.4	**0.95 (0.82 0.98), 0.0005***
PVS median short axis (mm)	3.1 (0.1)	3.1 (0.07)	0.5	**0.95 (0.82 0.98), 0.0005***

*Supplementary Table B: Summary table of absolute PVS measures from PVSSAS with manual edits performed on 2008 scans and then the same manual editing process on the same scans a week later. Values reported are means and standard deviations. The percentage difference is the absolute mean percentage difference between scans for each variable. A two-way mixed-effects ICC model was used to assess the reproducibility of manual edits on same-scan data. The cohort included a mixture of healthy controls and HD participants (n=12). *Statistically significant (p<0.05). Abbreviations: ICC, intra-class correlation; CI, confidence interval.*

ICC values for all PVS metrics were 0.95 or higher, showing excellent reproducibility of the manual refinement process for all PVS measures (Supplementary Table B) including only an absolute mean percentage difference of 2% in PVS count and 6.7% in PVS volume.

Test 2: Scan-rescan reproducibility on healthy control data, one year apart, without manual edits:

The ICC reliability results for the scan-rescan reproducibility on PVSSAS output from healthy control scans acquired one year apart, without editing PVS segmentations are represented in Supplementary Table C. This includes ICC estimates and 95% CI.

Supplementary Table C – PVSSAS reproducibility without manual intervention on healthy control data of PVS metrics (Test 2).

	2008 (n=12) Mean (SD)	**2009 (n=12) Mean (SD)**	**Mean absolute % difference**	**ICC (95% CI), p**
PVS count	273 (40.1)	283 (45.5)	7.1	**0.88 (0.64 0.96), 0.0005***
PVS total volume (mm^3)	6309 (1253)	6353 (1360)	5.1	**0.95 (0.85 0.99), 0.0005***
PVS median long axis (mm)	5.2 (0.3)	5.0 (0.2)	5.8	0.4 (-0.2 0.8), 0.086
PVS median short axis (mm)	3.4 (0.1)	3.3 (0.1)	3.6	-0.23 (-0.7 0.4), 0.77

*Supplementary Table C: Summary table with absolute PVS measures outputted from PVSSAS without manual intervention between paired 2008 and 2009 scans in healthy controls. Values reported are means and standard deviations. The absolute percentage difference is the absolute mean percentage difference between 2008 and 2009 results for each PVS metric. A two-way mixed-effects ICC model was used to assess scan-rescan reproducibility for outputted PVSSAS metrics without manual edits. *Statistically significant (p<0.05). Abbreviations: ICC, intra-class correlation; CI, confidence interval.*

The test-retest reliability of PVSSAS without manual intervention indicates excellent reproducibility for PVS total count and PVS total volume (ICC of 0.89 and 0.94, respectively). However, this reproducibility was not reflected for PVS median long- and short-axis which showed poor ICC reliability

on scan-rescan longitudinal data (0.4 and -0.23, respectively), despite the mean PVS median long- and short-axis for 2008 and 2009 scans being very similar (long-axis: 5.2mm and 5.0mm, respectively and short-axis: 3.4mm and 3.3mm, respectively) and the absolute mean percentage difference between the scans for each PVS length was low (5.8% and 3.6%, respectively).

Test 3: Scan-rescan reproducibility on healthy control data, one year apart, with manual edits:

The reliability results for the scan-rescan reproducibility of the PVSSAS output on healthy control data one year apart, but with the addition of manually refining PVS segmentations, are shown in Supplementary Table D. This includes ICC estimates and 95% CI.

Supplementary Table D – PVSSAS reproducibility with manual intervention on healthy control data of PVS metrics (Test 3).

	2008 (n=12) Mean (SD)	**2009 (n=12) Mean (SD)**	**Mean absolute % difference**	**ICC (95% CI), p**
PVS count	223 (67)	235 (68)	7.8	**0.96 (0.88 0.99), 0.0005***
PVS total volume (mm^3)	3775 (1572)	3934 (2019)	11	**0.92 (0.77 0.98), 0.0005***
PVS median long axis (mm)	4.2 (0.31)	4.1 (0.33)	5.9	**0.62 (0.1 0.87), 0.0012***
PVS median short axis (mm)	3.1 (0.1)	3.1 (0.1)	2.9	0.37 (-0.23 0.76), 0.11

Supplementary Table D: Summary table with absolute PVS measures outputted from PVSSAS with manual intervention between paired 2008 and 2009 scans in healthy controls. Values reported are means and standard deviations. The absolute percentage difference is the absolute mean percentage difference between 2008 and 2009 results for each PVS metric. A two-way mixed-effects ICC model

*was used to assess scan-rescan reproducibility for manual edits between 2008 and 2009 scans. *Statistically significant (p<0.05). Abbreviations: ICC, intra-class correlation; CI, confidence interval.*

The ICC results for this reproducibility test reflect similar results as those without manual intervention (Test 2) with excellent reliability for PVS total count and PVS total volume (ICC 0.96 and 0.92, respectively). However, the absolute mean percentage differences for PVS count and PVS volume were higher (7.8% and 11%, respectively) compared to those without manual intervention (Test 2, Supplementary Table C). This reproducibility test showed slightly improved ICC estimates for PVS median long-axis with moderate reliable reproducibility (ICC 0.62). PVS median short-axis still showed poor reliable reproducibility with 0.37 ICC.

From the PVS length results in Test 2 and Test 3, there was low confidence in PVSSAS output for PVS length measures, therefore PVS length was not assessed in the main analysis.

Supplementary Table E - Relationship between PVS measures and HD disease burden and severity measures.

		PVS total count (per 1000 mm^3 WMV)	PVS total volume (% of WMV)
DBS	Coefficient (95% CI), *p*	0.0001 (-0.0002 0.0005), 0.56	0.0001 (-0.001 0.001), 0.85
TMS		0.002 (-0.003 0.007), 0.37	0.012 (-0.004 0.03), 0.15

Supplementary Table E: Linear regression results from PVS count density and PVS volume (as a percentage of white matter volume) between DBS in both HD groups combined and TMS in early-HD participants only. All models adjusted age, sex, and TIV as nuisance variables. Abbreviations: WMV, white matter volume; DBS, disease burden score; TMS, total motor score; CI, confidence interval.